Materials and Design 204 (2021) 109645

Contents lists available at ScienceDirect

Materials and Design

journal homepage: www.elsevier.com/locate/matdes

Evolution of internal pores within AlSi10Mg manufactured by laser powder bed fusion under tension: As-built and heat treated conditions

James C. Hastie [a], Joachim Koelblin [a], Mehmet E. Kartal [a,*], Moataz M. Attallah [b], Rafael Martinez [b]

[a] School of Engineering, University of Aberdeen, UK
[b] School of Metallurgy and Materials, University of Birmingham, UK

HIGHLIGHTS

- A combination of X-ray tomography and micro-testing has demonstrated a powerful solution for characterizing *in-situ* microvoid growth and coalesce in aluminium alloy AlSi10Mg.
- Process conditions (as-built, hot isostatic pressing (HIP) and HIP+T6) have shown a significant impact on 3D pore evolution within AlSi10Mg.
- Under tensile deformation, microvoids in the as-built condition do not change markedly while the most substantial change occurs in the HIPped material

GRAPHICAL ABSTRACT

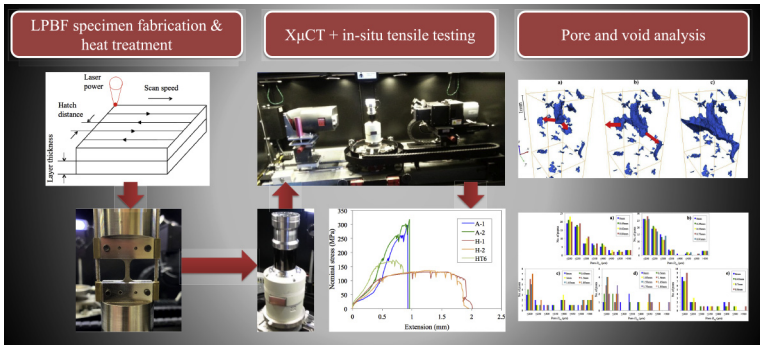

ARTICLE INFO

Article history:
Received 23 September 2020
Received in revised form 7 February 2021
Accepted 5 March 2021
Available online 9 March 2021

Keywords:
Laser powder bed fusion
Selective laser melting
Tensile testing
Internal porosity
in-situ X-ray micro computed tomography

ABSTRACT

The optimisation of processing parameters to produce high densification AlSi10Mg parts by laser powder bed fusion (LPBF) has received considerable attention in recent years. Nonetheless, it is important to consider the potential presence of as-built large pores in real world applications, *e.g.* due to limitations of the available LPBF system, time and cost constraints associated with producing near-perfect density and so on. In this work, recycled powder was used to fabricate AlSi10Mg specimens with sub-optimal densification by LPBF and an experimental investigation into the evolution of specimen porosity occurring under increasing tensile load was performed. A combination of high-resolution X-ray micro computed tomography (XμCT) and an *in-situ* micro-testing stage was employed to acquire 3D images at different loading stages. Specimens were tested in the as-built condition and following hot isostatic pressing (HIPping) or HIPping with T6. As-built porosity did not change markedly in the lead-up to brittle-like fracture. Pores within ductile HIPped specimens were uniformly elongated up to the onset of damage propagation and pore coalescence. Pore shape change occurred largely without volume change at small extension. HIPping plus T6 produced a compromise between as-built and HIPped conditions in terms of the extent of pore modification observed prior to failure.

1. Introduction

Laser powder bed fusion (LPBF), also broadly referred to as 'selective laser melting (SLM)', is a popular metal powder additive manufacturing (AM) technique in which 3D parts are produced by fusing pre-deposited metal powder using a high-energy laser beam. In industrial sectors including medical, aerospace and automotive, LPBF is becoming increasingly prevalent for the ability to fabricate near-net shape engineering parts directly from a computer aided design (CAD) model, therefore providing robust design flexibility without the limitations of traditional manufacturing techniques that necessitate a series of steps

* Corresponding author.
E-mail address: mehmet.kartal@abdn.ac.uk (M.E. Kartal).

https://doi.org/10.1016/j.matdes.2021.109645

(each requiring requisite material consumptions, energies and costs) [1,2].

With very high strength-to-weight ratio, corrosion resistance and thermal conductivity, heat treatable Al—Si alloys are widely used in aerospace and automotive applications. The Al—Si alloys can be strengthened, without changing other mechanical properties, by adding Mg due to the precipitation of Mg_2Si. AlSi10Mg is one of the most commonly used Al—Si alloys, traditionally manufactured by die casting. However, casting requires part-specific tooling with cost and lead time implications. Furthermore, this process results in large grains with poor mechanical response (in view of the Hall-Petch relationship) as a result of low cooling rates [3]. As such, manufacturers are constantly striving to develop new cost-effective techniques to produce parts with enhanced accuracy.

Silicon content in AlSi10Mg makes composition near eutectic and inhibits solidification cracking. It is known that the presence of Si in this alloy improves the fluidity of molten aluminium. Furthermore, Si has a narrow solidification range and absorbs laser [4,5]. These features make LPBF an ideal route for producing AlSi10Mg components with high densification if processing parameters used in LPBF are optimised [6].

The main influential parameters on densification in LPBF are the feedstock powder characteristics (powder size, morphology and size distribution) and energy density (a function of four different processing parameters: laser power, scanning speed, scan spacing and layer thickness) that regulates the degree of powder particles to be consolidated [7]. In addition, unlike other metallic materials (*e.g.* titanium, steel and nickel), laser processing of aluminium can be challenging due to high reflectivity that necessitates the use of high laser powers for melting [5], and high thermal conductivity that causes rapid dissipation of heat from the scanned area [8]. These factors can stimulate porosity in fabricated parts. To address this, the influences of processing parameters and build conditions on internal porosity of AlSi10Mg fabricated by LPBF have been the subject of extensive research in recent years. Such interdependency was often investigated by altering a single process parameter while holding other influential variables constant. It has been found that porosity within LPBF-fabricated Al alloys is formed by a number of mechanisms. Residual gases or gases that become trapped during processing form small spherical pores (<100 μm) [9–11]. Excessive laser energy can cause localised vaporisation and formation of spherical "keyhole" pores deep within solidified melt pools [7,10,11]. Keyhole porosity can manifest as irregular (non-spherical) shapes with rapid solidification and instability [7,9,10]. Large irregular pores are created between adjacent powder layers when there is insufficient laser energy or scanning overlap for effective fusion [9,10]. Oxide films present in the powder or introduced under certain processing conditions can also prevent consolidation and result in irregular defect formation [7,8,12,13].

The effects of typical aluminium heat treatments, including hot isostatic pressing (HIPping) and T6 (solutionising and artificial ageing), on porosity and mechanical performance of LPBF-fabricated AlSi10Mg have been investigated (*e.g.* [14–20]). When compared to the cast counterpart, the LPBF-fabricated alloy exhibits superior mechanical strength due to microstructure refinement by rapid solidification [10,21–23]. Post-treatments cause coarsening of the microstructure that reduces ultimate tensile strength (UTS) and hardness whilst it increases ductility [21–23]. Densification of the as-built material can be improved considerably by HIPping, which collapses micro-pores [11,12,20].

With regards to pore characterisation, porosity has frequently been analysed using traditional cross-sectioning and 2D imaging methods, *e.g.* optical microscopy (OM) and scanning electron microscopy (SEM) on cut and polished specimen surfaces (*e.g.* [7,9,10,24,25]). With these approaches, only those pores at the free surface can be characterised and no information is provided on the sub-surface condition where pore-morphology may differ. As pores possess complex morphologies and can be responsible for material failure mechanisms their evaluation should be made in 3D. Hence, there is now an increasing trend in the use of X-ray micro computed tomography (XμCT) for analysing internal pores [26–28]. The use of XμCT in conjunction with image analysis software allows efficient evaluation of internal pore frequency, volume fraction, location and size/shape in 3D [11,12,29,30]. Moreover, XμCT affords the ability to directly incorporate microstructural features (*i.e.*, size and position of voids) into finite element models without having to approximate or assume internal features (*e.g.*, [31]). It should be noted that porosity measured using XμCT can be significantly higher than estimates obtained using 2D imaging methods due to the ability to characterise finer pores [12,32].

In existing literature, the mechanical properties of AlSi10Mg parts have generally been measured using conventional experimental rigs. Such procedures give the global mechanistic response without revealing internal failure mechanisms. A material's mechanical response is controlled by microstructure and deformation at the microscale level. It has been theoretically and numerically well documented that ductile failure occurs under the effect of void nucleation, void growth, and void coalescence [33–36]. Since porosity can play a significant role in failure, investigating 3D micro-level damage mechanisms of internal porosity under mechanical loading is an important engineering task. This type of *in-situ* experimental work is scarce in the literature. Whilst there have been many studies aimed at optimising LPBF processing parameters for the production of high densification AlSi10Mg parts and understanding their mechanical performance, one must consider that highly optimised processing may not always be feasible in a real world scenario, *e.g.* due to limitations of the available LPBF system or economic constraints, and the presence of large pores may be unavoidable. The *in-situ* study of sub-optimal AlSi10Mg parts is therefore also of practical importance.

In very recent years, there have been a few studies where the combination of XμCT and an *in-situ* micro-testing stage was employed to study damage mechanisms in LPBF fabricated stainless steel [37,38] and Cu—Sn alloy [39]. Recently, Samei et al. [40] studied the evolution of pores in a single untreated AlSi10Mg specimen using *in-situ* XμCT scanning at incremental levels of tensile strain. In the present paper, *in-situ* tensile testing with XμCT was performed on LPBF-fabricated AlSi10Mg specimens in as-built (untreated), HIPped and HIPped plus T6'd conditions. Void accumulation and shape change at increasing tensile extension are evaluated for each condition. The specimens were fabricated using recycled powder (known to result in sub-optimal densification [32]) in order to study the evolution of lack-of-fusion defects of worst-case size. This follows recent works involving *ex-situ* mechanical testing [15] and fatigue modelling [41] of similarly sub-optimal AlSi10Mg. We believe this is the first time the application of XμCT with *in-situ* micro-testing for the characterisation of damage mechanisms in thermally treated AlSi10Mg has been reported in literature.

2. Experimental methods

2.1. Materials, processing and heat treatments

AlSi10Mg blocks of 20 mm thickness were manufactured in an argon environment (oxygen content 100 ppm) using a Concept Laser M2 Cusing system at the University of Birmingham. Composition of the alloy powder (size range 15-53 μm) supplied by LPW Technology is given in Table 1. The powder, which has similar non-spherical morphology to the powder studied by Read et al. [7], was recycled for processing. The blocks were processed using the following LPBF parameters: 150 W laser power; 500 mm/s scanning speed; 45 μm scan spacing; 30 μm powder layer thickness. We note that these parameters were selected based on the previous study [11] and are unlikely to be transferable

Table 1
AlSi10Mg composition (Wt%).

Al	Si	Mg	Fe	Ni	Zn	Ti	Mn	Pb	Sn
Bal.	9.92	0.291	0.137	0.04	0.01	0.006	0.004	0.004	0.003

(*i.e.* giving full consolidation) even with fresh powder. However, we reiterate the aim of this work is to investigate void growth and coalescence rather than process optimisation or void nucleation (resolution of XμCT is not suitable for this early stage of damage mechanism in any case), therefore sub-optimal densification was deemed appropriate.

Blocks, as opposed to final specimen geometries, were initially fabricated as thin test specimens may be particularly susceptible to surface defects. The specimens were then machined from the blocks. Since the dimensions are several times smaller than those of conventional tensile testing specimens, machining methods may significantly affect mechanical properties and roughness. Electro discharge wire machining (EDM) appears to be an effective method for extracting a miniature specimen [42,43] and was employed for this aim. EDM, a non-contact method, utilises an electrically charged thin wire to remove material and hence cutting-related residual stress is expected to be insignificant [44]. EDM also provides good shape tolerance and surface finish. The cutting-affected depth with EDM is around 125 μm from the cut surface [45]. Nominal specimen geometry, shown in Fig. 1, was dimensioned to suit the *in-situ* tensile testing machine described in Section 2.2. Specimen blocks were built in the thickness (*Y*) direction by raster scanning in the transverse (*XZ*) plane. Island scanning strategy of 5×5 mm^2 was used. For heat treatment of machined specimens, standard HIPping and T6 procedures for AlSi10Mg were used, summarised in Table 2.

In order to firstly determine critical deformation stages at which X-ray scans would be acquired during *in-situ* tensile testing, an *ex-situ* (uninterrupted) tensile test was performed for samples in as-built, HIPped and HIPped + T6'd conditions. Samples were strained until failure using a Deben CT5000 testing stage. Nominal stress *vs.* extension curves for preliminary *ex-situ* tensile tests are shown in Fig. 2. Note that extension values were measured based on the machine cross head and therefore involve the combined effect of actual deformation and compliance of the Deben machine. Therefore, the plots show non-linear curve in the elastic zone, which is not uncommon for *in-situ* X-ray testing in tensile mode [38]. The as-built material achieves a high maximum load but it is the most brittle. Heat treatment lowers the tensile strength and increases ductility, as has been previously observed [12,14–16,18,21–23]. Extension to failure measured by the cross head is more than twice in comparison with the as-built material. The mechanical response of the HIPped + T6'd condition can be regarded as a compromise between as-built and HIPped in terms of strength and ductility. The UTS of the as-built, HIPped and HIPped + T6'd specimens was calculated as 320 MPa, 130 MPa and 162 MPa respectively. Fractured specimens are also shown in Fig. 2.

2.2. In-situ tensile testing

Following the *ex-situ* tests, two specimens were subjected to *in-situ* testing in each condition. Due to a disruption during *in-situ* testing of the HIPped + T6'd specimens the results were recorded for a single specimen only. However, as the *in-situ* results (shown in Section 3) were consistent with the preliminary *ex-situ* test (Fig. 2), and given that time and cost are very high for interrupted testing, further experiments were not deemed essential. In the as-built and HIPped cases, repeatability for the pairs of specimens was very strong. The two as-built, two HIPped and single HIPped + T6'd specimens are referred to herein as A-1, A-2, H-1, H-2 and HT6 respectively.

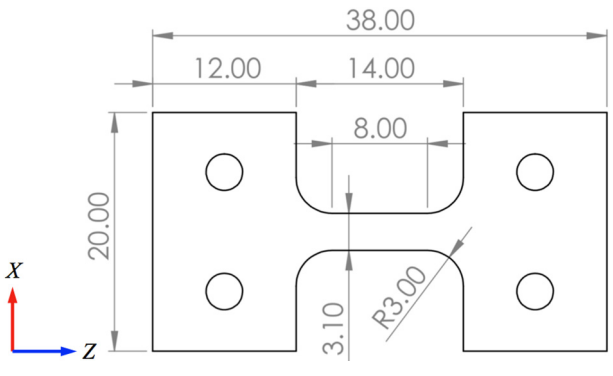

Fig. 1. Nominal tensile specimen dimensions in mm (3.10 mm *Y* thickness); specimen symmetric about centre planes.

Table 2
Heat treatment parameters.

HIPping	T6
2 h @ 500 °C / 100 MPa 5 °C/min heating/cooling	5 h @ 530 °C Water quench 8 h @ 160 °C Air cooling

Tensile testing was performed using a Deben CT5000 *in-situ* testing stage in conjunction with XμCT. The X-ray microscope used in this work was the ZEISS VersaXRM-410, which has a minimum spatial resolution of 0.9 μm, minimum voxel size of 0.1 μm, maximum power output of 10 W and maximum voltage of 150 kV [46]. The CT5000 used has a maximum 5kN tensile/compression load capacity, maximum extension of 10 mm and motor speed range of 0.1-1 mm/min [47]. The experimental setup is shown in Fig. 3. The combination of the VersaXRM-410 and CT5000 machine has been previously tested (*e.g.* for syntactic foam; more information can be found in the work of Kartal et al. [48]). The sample was mounted into the machine's jaws, housed within a 3 mm thick vitreous glassy carbon tube that provides low X-ray attenuation. Tensile testing was operated under displacement control at the ambient temperature. The extension was kept constant at the targeted value during XμCT scanning, before being increased to the next target scanning point, and so on. The first scan of each test was taken at a very light load in order to capture the unstrained configuration of internal pores. The strain levels for subsequent scans were determined using the results obtained from *ex-situ* testing (Fig. 2). Applied extension and load were controlled and recorded by means of Deben stage control software. Note that specimen dimensions were specifically chosen to ensure that the specimens could be loaded beyond UTS whilst the capacity of the load cell (5kN) would not be exceeded, and that elongation to failure would occur within the maximum extension limit of the machine. Reducing the sample cross section would not significantly improve scan time and would increase the risk of plastically deforming the gauge length during setups. Therefore, a smaller cross section was not preferred.

Each scan was performed using a beam energy of 140 kV (140 keV x-ray photons) and a power of 10 W. An optical magnification of 4× was used to achieve high resolution images. The pixel size was set to be 2.86 μm for a 1024×1024 pixel projection image that provides a cylindrical field-of-view (FOV) with 2.9 mm diameter and length. In order to obtain the best signal-to-noise ratio, a minimum of 5000 intensity values on each projection was required [46]. Since aluminium density is lower than many other high-Z alloys, a relatively short exposure (12 s) was sufficient. A total of 2400 projections over 360° rotation was acquired for each scan. It should be noted that higher resolution (*e.g.*, 1 μm pixel resolution) could have been achieved with the same FOV but this would increase scan time by a factor of four for every two times better pixel resolution. Similarly, higher pixel size resolution with a smaller FOV directly affects the exposure time. Considering time and cost associated with a number of scans in this work, the scan setups were deemed to give the optimum high resolution for the tests conducted. It should be noted that the XμCT system used here can produce a larger field of view by using an alternative lens (*i.e.*, 0.4×). This option would produce low-resolution tomography useful for inspection purposes or optimising process parameters with relatively short scanning time

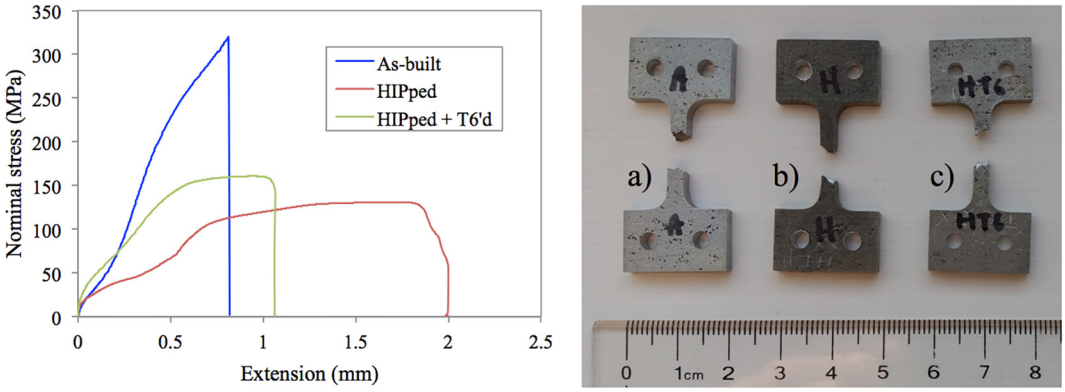

Fig. 2. *Ex-situ* nominal stress *vs.* extension for as-built and treated specimens (left); fractured *ex-situ* specimens (right): as-built (a), HIPped (b) and HIPped + T6'd (c) (figure available in colour online).

(~1 h per scan). However, such experimental set-up would not permit investigation of damage accumulation of pore size below 100 μm. Strategies for effective use of XμCT were discussed elsewhere [26].

At each stage of deformation, scans were performed at three different locations within the specimen gauge length: adjacent top, middle and bottom sections with 2.9 mm length to ensure internal void evolution was fully visible along the entire gauge length. Fig. 4 shows the scanning locations. Xradia XMReconstructor software was used to reconstruct 2D radiographs into 3D and beam hardening and centre shift artefacts were removed.

2.3. Image processing

The software Avizo 9 was used to analyse internal porosity by thresholding XμCT images taken at incremental specimen extensions. Analysis was performed on a discrete 650 × 650 pixel (px) cross-section (with axes *x* and *y*) within the circular FOV along the full length (*z* axis). A non-local means filter was applied and features smaller than 1px were neglected. For quantitative porosity analysis the top, middle and bottom scans were combined into a single image using the merge feature on Avizo. To evaluate the evolution of pore geometry under load we consider changes in 3D Feret caliper descriptors, shown in Fig. 5. The Feret dimensions D_{max}, D_{min} and D_{med} of a particle are the maximum length, corresponding minimum width belonging to the same plane and maximum breadth orthogonal to the width respectively. As measurements depend on orientation, the maximum length and corresponding width/breadth were determined based on the Avizo's default 31 directions for Feret analysis.

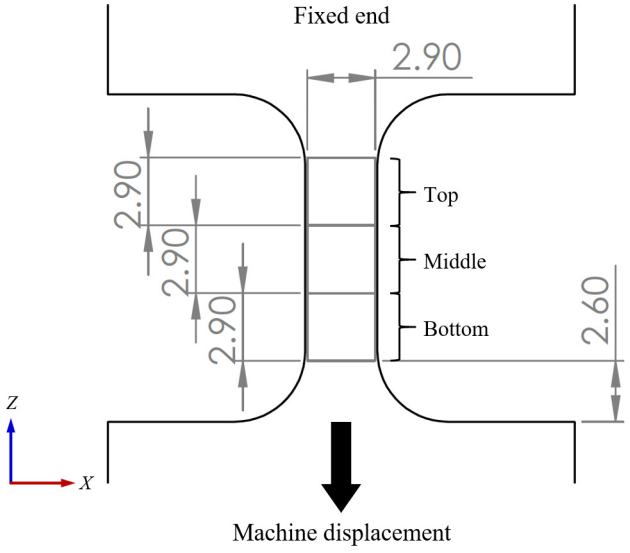

Fig. 4. Specimen scanning locations (dimensions in mm).

3. Results and discussion

3.1. Void accumulation

Internal porosity volumes for *in-situ* specimens at 0 mm extension are given in Table 3. Maximum pore equivalent diameters are also

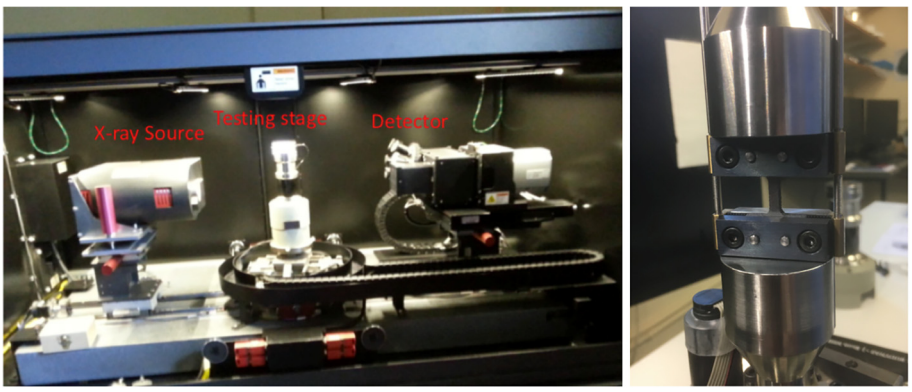

Fig. 3. *In-situ* tensile testing setup (left); specimen fixed into machine jaws (right).

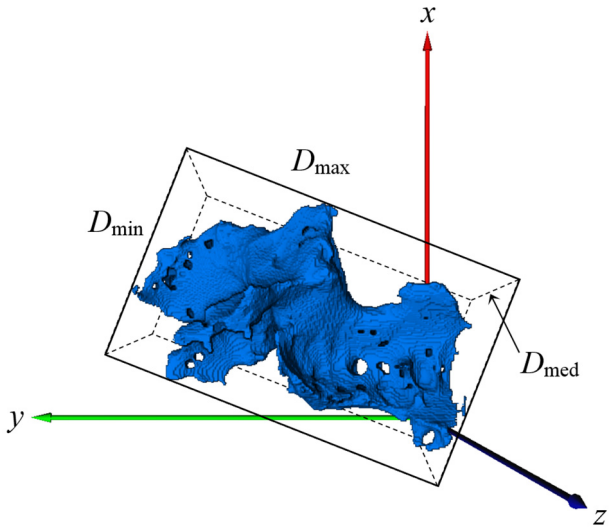

Fig. 5. Pore Feret caliper 3D descriptors.

Table 3
In-situ specimen porosity (0 mm extension).

Specimen	Porosity (%)	Max. pore D_{eq} (μm)
A-1	3.87	603.98
A-2	3.26	667.76
H-1	1.10	580.79
H-2	0.28	382.43
HT6	0.65	426.21

shown in Table 3. The equivalent diameter (D_{eq}) is regularly used to quantify pore size and is the diameter of a sphere of equivalent volume, *i.e.*:

$$D_{eq} = \sqrt[3]{\frac{6V_{pore}}{\pi}}, \quad (1)$$

in which V_{pore} is the pore volume determined with the help of 3D image thresholding software. The as-built specimens involve 3–4% porosity. As explained, recycled powder was used for fabricating specimens with significant porosity for examination. A very similar as-built quality (96.4% densification) was reported by Kan et al. [15] in their *ex-situ* investigation on sub-optimal AlSi10Mg. Densification increases with post-thermal treatments. HIPping collapses pores and improves densification, whilst subsequent T6 causes some void reopening. Specimen H-1 exhibits unusually high porosity (1.10%), *i.e.* markedly higher than H-2 (0.28%) and higher than the HIPped + T6'd specimen (0.65%). This is attributed to the presence of large pores that could not be collapsed by HIPping, possibly due to sensitivity to pore size [11] or alternatively due to pore connections with the specimen surface preventing closure. The size of the largest pore in H-1 is notably greater than H-2. Interestingly, this afforded the opportunity to study the influences of larger pores and increased porosity on tensile response. It should be noted that porosity analysis performed at 0 mm extension in this work was not intended to show the effects of the heat treatment on the size, shape and volume of pores. In other words, the porosity of H-1, H-2 and HT6 samples prior to the heat treatments was not measured. Such analysis can be found elsewhere [11].

In-situ nominal stress *vs.* extension curves (consistent with the *ex-situ* tests) and fractured specimens are shown in Fig. 6 (calculating true strain from the extension would only be possible if the FOV included the entire cross section (*e.g.* [39])). Strong repeatabilty is evident for the as-built and HIPped specimen pairs. We observe the curves are virtually identical for the HIPped specimens up to fracture, despite noticeable difference in initial porosity, *i.e.* the larger porosity did not have an appreciable effect on tensile capacity. All specimens were split through the middle region. The sudden drops along the curves correspond to the points during each test at which extension was kept constant and XμCT scans were carried out. Immediately after testing was interrupted there was a noticeable drop from the targeted scan point; some noise following the initial drop corresponds to the samples being loaded several times within a short period of time (~10mins) until the change in targeted test value became insignificant prior to the scan. In addition, stress relaxation still occurs for a constant displacement value over time, particularly in the plastic deformation zone due to energy dissipation and this brings about a decrease in the stress value required to hold the same amount of strain. Given that each scanning set (top, middle and bottom) took approximately 24 h to complete, further stress relaxation could occur, changing the internal structure of the material and thus distorting the image produced. To account for this, samples were left at a constant level of extension for a period of 1 h before each scan was conducted, thereby mitigating any negative effect on the scanned image quality [48].

Damage accumulation *vs.* extension for combined and individual sub-volumes obtained from each test sample is shown in Fig. 7. Volume fraction within A-1 and A-2 did not change appreciably under tension up to the final scans. Some minor variation is attributed to shifting of pores in/out of the analysis frame with extension. In H-1 the overall porosity volume remains constant from 0 to 0.45 mm before gradually rising to 1.65 mm as fractions in top and bottom sub-volumes increase. There is subsequently a sharp increase as damage accumulates primarily in the middle section. *In-situ* testing of H-2 was performed with additional scanning increments at the late stage of deformation, showing

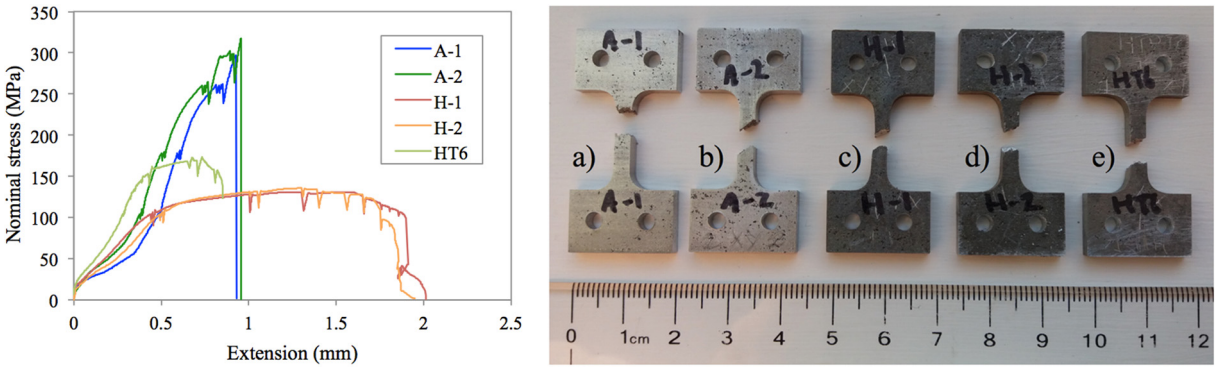

Fig. 6. *In-situ* nominal stress *vs.* extension for all specimens (left); fractured *in-situ* specimens (right): A-1 (a), A-2 (b), H-1 (c), H-2 (d) and HT6 (e) (figure available in colour online).

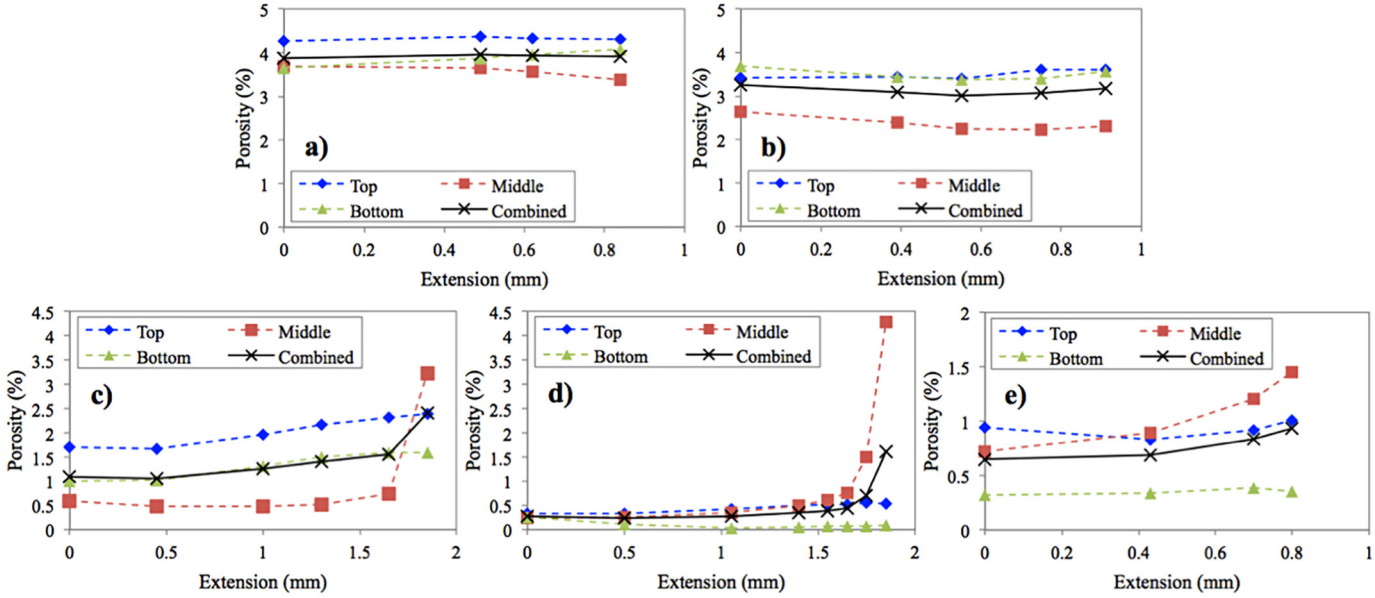

Fig. 7. Porosity volume *vs.* extension: A-1 (a), A-2 (b), H-1 (c), H-2 (d) and HT6 (e) (figure available in colour online).

an exponential increase in porosity through the middle section where fracture occurred. Overall porosity in HT6 increases with extension, namely due to a rise in the middle section where damage propagated, but a sharp secondary increase is not observed at the final scanning point. Volume fraction does not increase in top and bottom locations away from the damage epicentre.

Figs. 8 and 9 show the frequency distributions of pores with $D_{eq} > 25$ μm in the merged volumes of all tested specimens at increasing extension (results are split across two figures for axis readability; A pore size of $D_{eq} > 25$ μm, which is <10× the pixel size of 2.86 μm, is considered as geometric measurements of very small features that are especially sensitive to thresholding are inherently unreliable. Pores with $D_{eq} \leq 25$ μm contribute to <1% of the total volume in all specimens prior to loading and were deemed to be negligible). As-built specimens contain a large number of pores at 0 mm and distributions of pores with $D_{eq} \leq 150$ μm do not vary significantly with extension. Some minor fluctuation in quantities of small pores, more noticeable in A-1, may be attributed to shifting in/out of the FOV during tensile loading. In both specimens there is also some fluctuation in the number of pores with D_{eq} between 150 and 500 μm (particularly 250 and 300 μm) under tension. This is thought to be caused by the close proximity of neighbouring pores in the highly porous specimens. Two separate pores that share a single voxel would be counted as one feature (no attempt to manually separate pores was made to avoid misinterpretation of results) but could be counted as two separate pores at subsequent extensions due to analysis sensitivity alone. As will be later shown visually, the

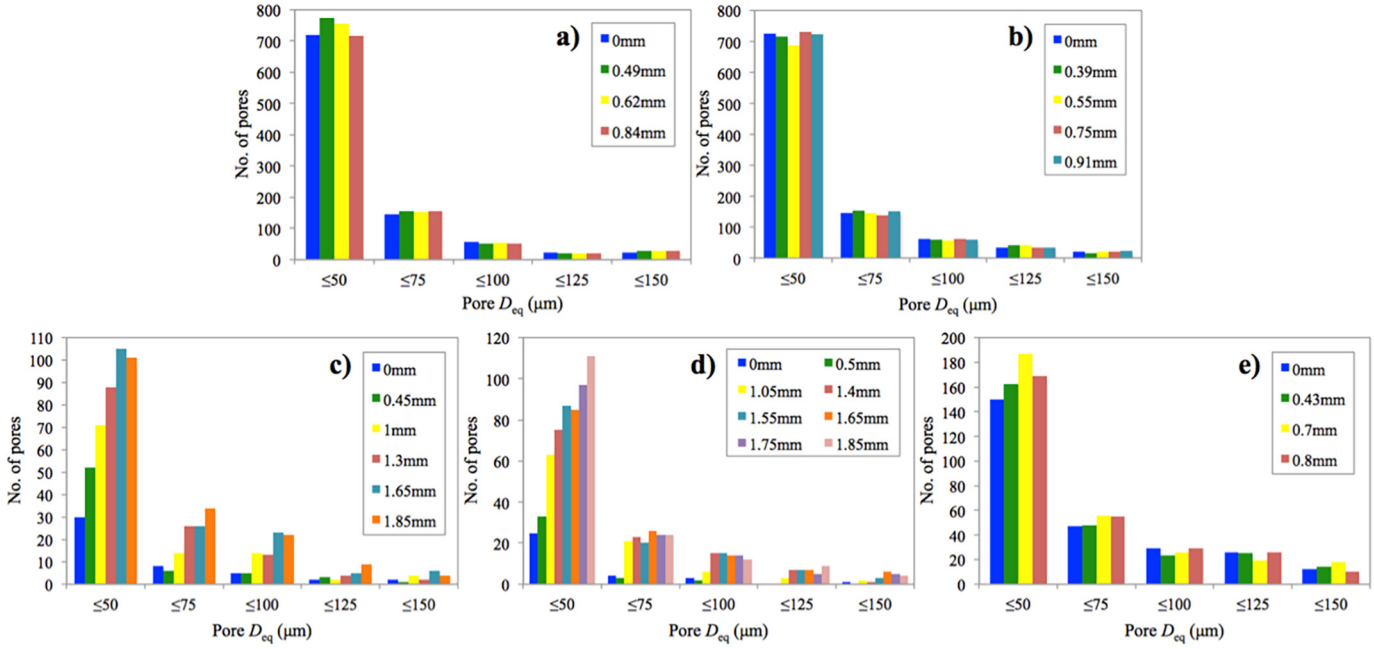

Fig. 8. Distribution of pores with 25 μm < D_{eq} ≤ 150 μm at increasing extension: A-1 (a), A-2 (b), H-1 (c), H-2 (d) and HT6 (e) (figure available in colour online).

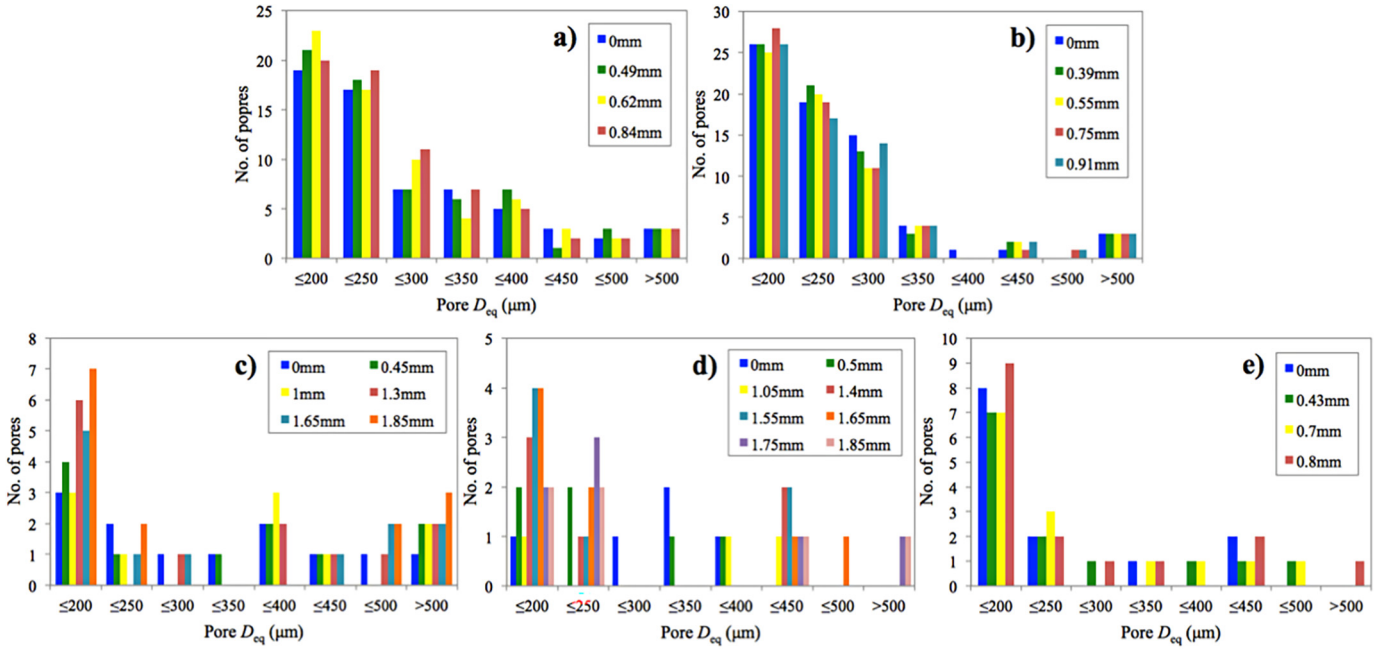

Fig. 9. Distribution of pores with D_{eq} > 150 μm at increasing extension: A-1 (a), A-2 (b), H-1 (c), H-2 (d) and HT6 (e) (figure available in colour online).

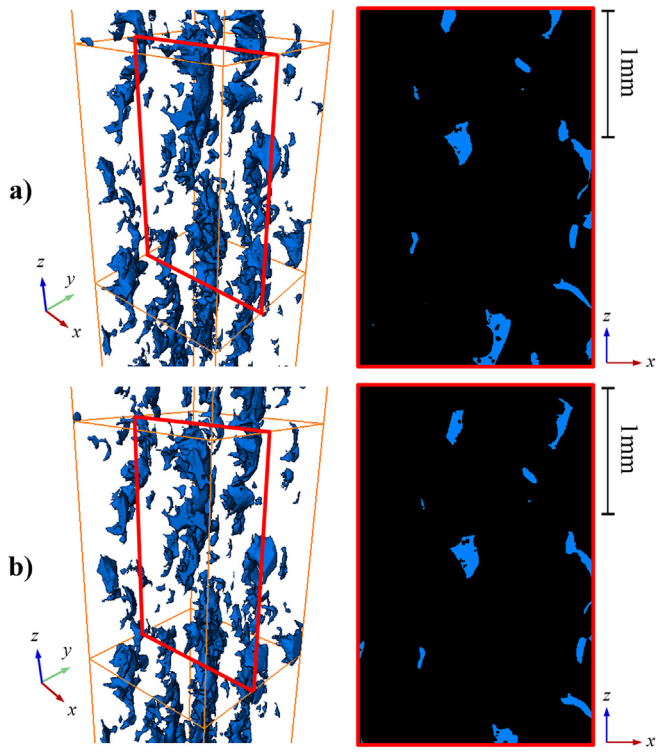

Fig. 10. Pores with D_{eq} > 50 μm in A-1 middle section at 0 (a) and 0.84 mm (b) extension.

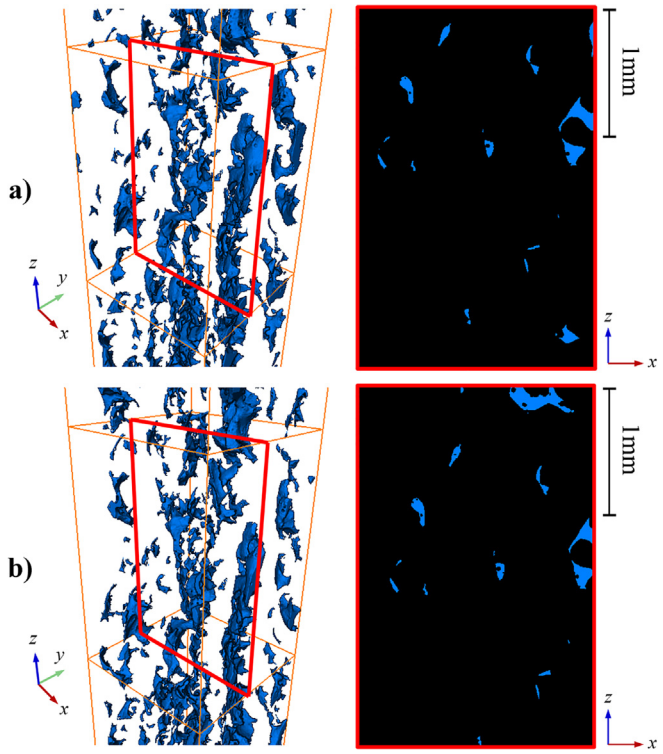

Fig. 11. Pores with D_{eq} > 50 μm in A-2 middle section at 0 (a) and 0.91 mm (b) extension.

morphology of pores does not change appreciably in A-1 and A-2, which agrees with unchanging porosity volume. There is no change in the number of large pores with D_{eq} > 500 μm in the as-built specimens. By comparison, HIPped specimens contain significantly fewer pores at 0 mm and there is a marked increase in size and overall frequency with extension. The frequency of pores with D_{eq} between 25 and 50 μm clearly rises, as nucleated new pores and/or pre-existing very small pores grow to detectable size under tension. Relative to 0 mm, H-1 and H-2 contain more than 3× and 4× the amount of pores in the 25 and50 μm range respectively at final extension. It is impossible to elucidate whether these newly detected pores were present prior to loading or introduced during specimen deformation, *e.g.* reopening of pores closed by HIPping. At D_{eq} = 250 μm and above, pores increase in size and coalesce under tension, resulting in a small number of very large pores at the final increment. We observe a higher number of large initial pores in H-1 relative to H-2 in the absence of loading.

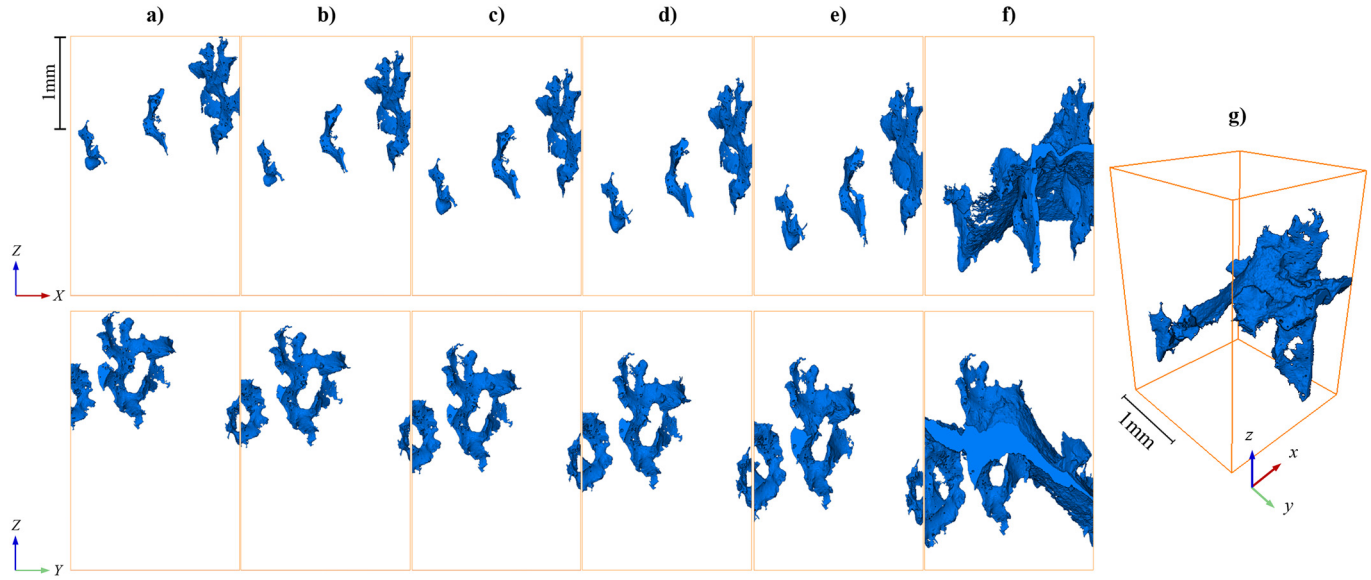

Fig. 12. Three largest initial pores in H-1 middle section at increasing extension (*xz* and *yz* views): 0 (a), 0.45 (b), 1.0 (c), 1.3 (d), 1.65 (e) and 1.85 mm (f); perspective view at 1.85 mm (g).

Ultimately however this did not appreciably alter the point at which significant damage began to accumulate, as seen in Fig. 7. HT6 contains greater initial quantity of pores than the HIPped specimens but fewer than the as-built specimens. The frequency of pores within HT6 appears to rise slightly with increasing extension, albeit not to a significant extent. This suggests that the rising number of detectable pores within HIPped specimens under tension is at least partly due to reopening of pores collapsed by HIPping; pores closed by HIPping may already have been reopened by T6 (hence a higher quantity prior to loading) and therefore a similar rise in quantity would not be observed during loading of HT6. Between 0.7 mm extension and the final scanning increment at 0.8 mm, the largest pore increases from $D_{eq} = 492.05$ to 544.55 μm, indicating pore growth. This was not accompanied by extensive pore coalescence, as will be later shown.

3.2. Pore shape change

Pores with $D_{eq} > 50$ μm in the middle section of A-1 and A-2 at initial and final extensions prior to fracture are shown in Figs. 10 and 11 respectively ($D_{eq} > 50$ μm is chosen for image clarity). Pores shift downwards through the sub-volume with extension, but morphology remains virtually unchanged (this can be observed clearly by comparing the 2D slices). This follows no appreciable variation in porosity volume fraction observed earlier in Fig. 7. We also see a number of very slender connections between large pores, which may be responsible for fluctuations in the numbers of 'individual' pores counted at different loading increments as earlier discussed. We note that the final scans were taken at approximately 90.5 and 95.3% of the failure extensions for A-1 and A-2 respectively. Thus, shape modification was not observed reasonably close to brittle fracture (it is impossible to capture the exact onset of fracture by means of interrupted testing). A brittle-like failure mechanism without significant change in pore shape at the final scan can be attributed to grain size refinement and process parameter dependent pile-up dislocation density that is particularly located at the grain boundaries in which further slips are hindered by the existing dislocation density. In addition, fine grains reduce the average distance between Si particles [21], which results in enhanced plastic strain gradient, and are obstacle for further slip, thus increasing sample strength and reducing ductility. Samei et al. [40] reported growth and coalescence of pores in their untreated AlSi10Mg specimen that exhibited a more

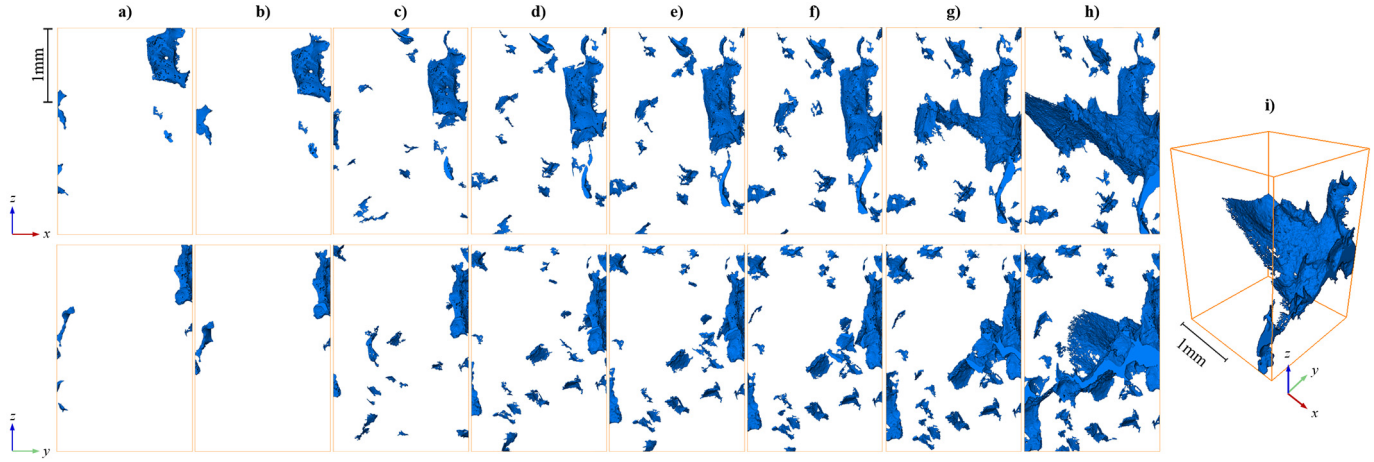

Fig. 13. Pores with $D_{eq} > 50$ μm in H-2 middle section at increasing extension (*xz* and *yz* views): 0 (a), 0.5 (b), 1.05 (c), 1.4 (d), 1.55 (e), 1.65 (f), 1.75 (g) and 1.85 mm (h); perspective view at 1.85 mm (i).

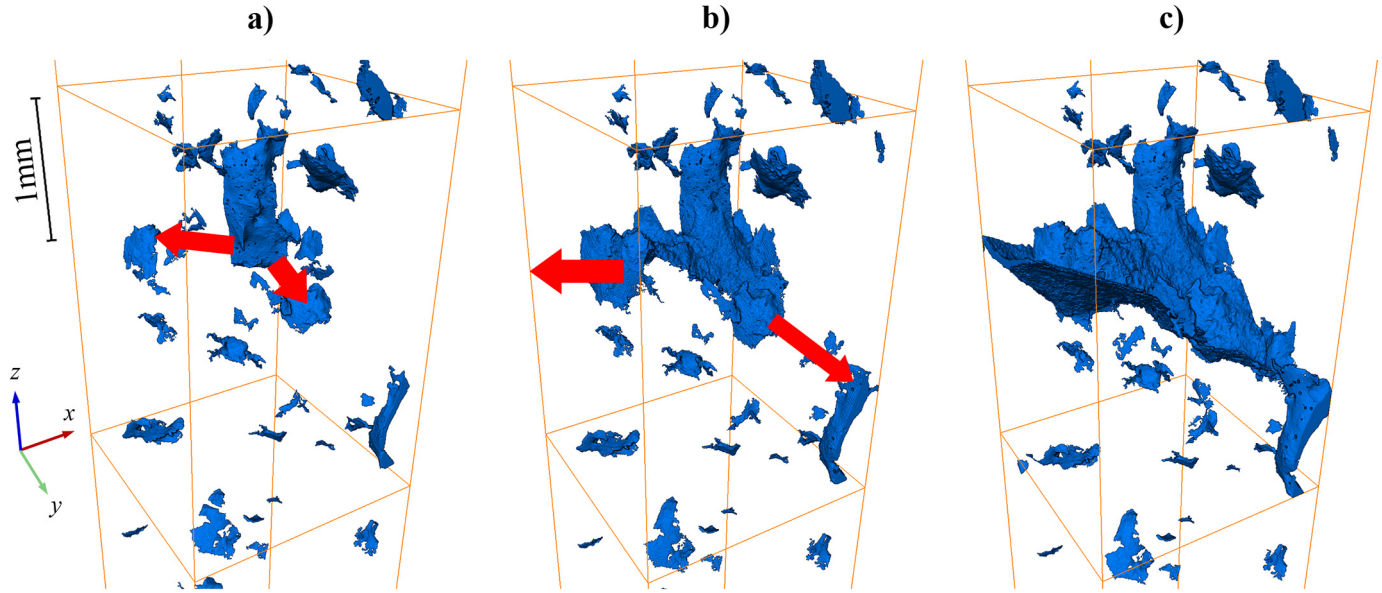

Fig. 14. Path of damage progression through H-2 middle section: 1.65 (a), 1.75 (b) and 1.85 mm (c) extension.

ductile response than the specimens examined here. Unloaded porosity was considerably lower than A-1 and A-2 (~0.05% at zero strain compared to >3%) and the mean pore diameter (~6 μm at zero strain) is below the size range considered in this study for thresholding reliability. However, dissimilar findings can be linked to differences in material ductility stemming from the use of different powder, LPBF processing parameters, build conditions *etc.*, as opposed to differences in pore volume and detectable size given that pores visibly evolved within denser HIPped specimens.

Internal porosity within H-1 and H-2 evolved clearly under tension. The three largest initial pores in the middle section of H-1 at increasing extension are shown from *xz* and *yz* views in Fig. 12. The pores remain isolated and are elongated in the loading (*z*) direction from 0 to 1.65 mm extension (with downward shifting under tension). The final scan at 1.85 mm before failure shows damage and coalescence of the pores. Samei et al. [40] observed similar coalescence by higher resolution scanning of their optimised untreated specimen devoid of pores of this magnitude. Fig. 13 shows pores with $D_{eq} > 50$ μm at increasing extension in the middle section of H-2. From 1.4 mm the number of visible features rises due to enlarging of pores previously below the detectable size or reopening of those closed by HIPping, as previously discussed. Significant damage has developed by 1.75 mm and progressed through the sub-volume at 1.85 mm. Although it is impossible to know the exact extension at which damage begins to accumulate, it is clear that coalescence had not commenced at 1.65 mm extension for either H-1 or H-2, *i.e.* at roughly 90% of the extension for the final scan that revealed significant damage. In other words, the onset of damage accumulation did not occur significantly earlier in H-1 with higher initial porosity and higher number of large pores. The path of damage progression from 1.65 to 1.85 mm within H-2 is shown in Fig. 14. Between 1.65 and 1.75 mm, damage propagates from the bottom of the largest pore and is terminated on the edges of neighbouring smaller pores at the point of scanning at 1.75 mm (this can also be seen from *xz* and *yz* views in Fig. 13f and g). This implies void growth occurred rapidly towards the pores and was temporarily captured. Increasing the extension to 1.85 mm then causes void growth to continue through the part thickness. The void appears to open at a declined angle towards a prominent pore in the vicinity below, which demonstrates significant pores can dictate the path of opening as it occurs. Hipping causes considerable reduction in dislocation density and results in more homogeneous microstructures, with Si particles randomly scattered in the Al-matrix and therefore solid solution strengthening is reduced. These microstructural changes make slip transfer easier under loading and hence void growth and coalescence can be clearly observed. Coalescence in HIPped

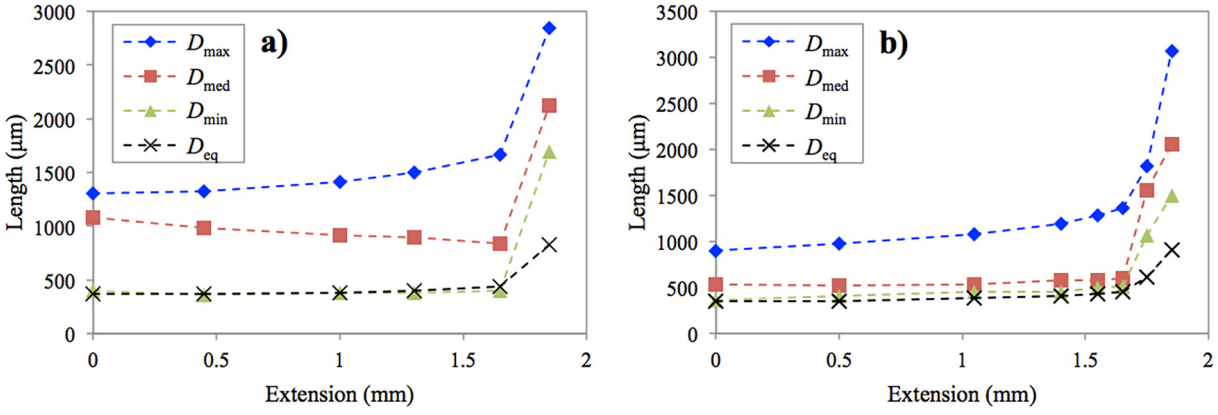

Fig. 15. Feret caliper dimensions of largest pore in middle section of H-1 (a) and H-2 (b) at increasing extension (figure available in colour online).

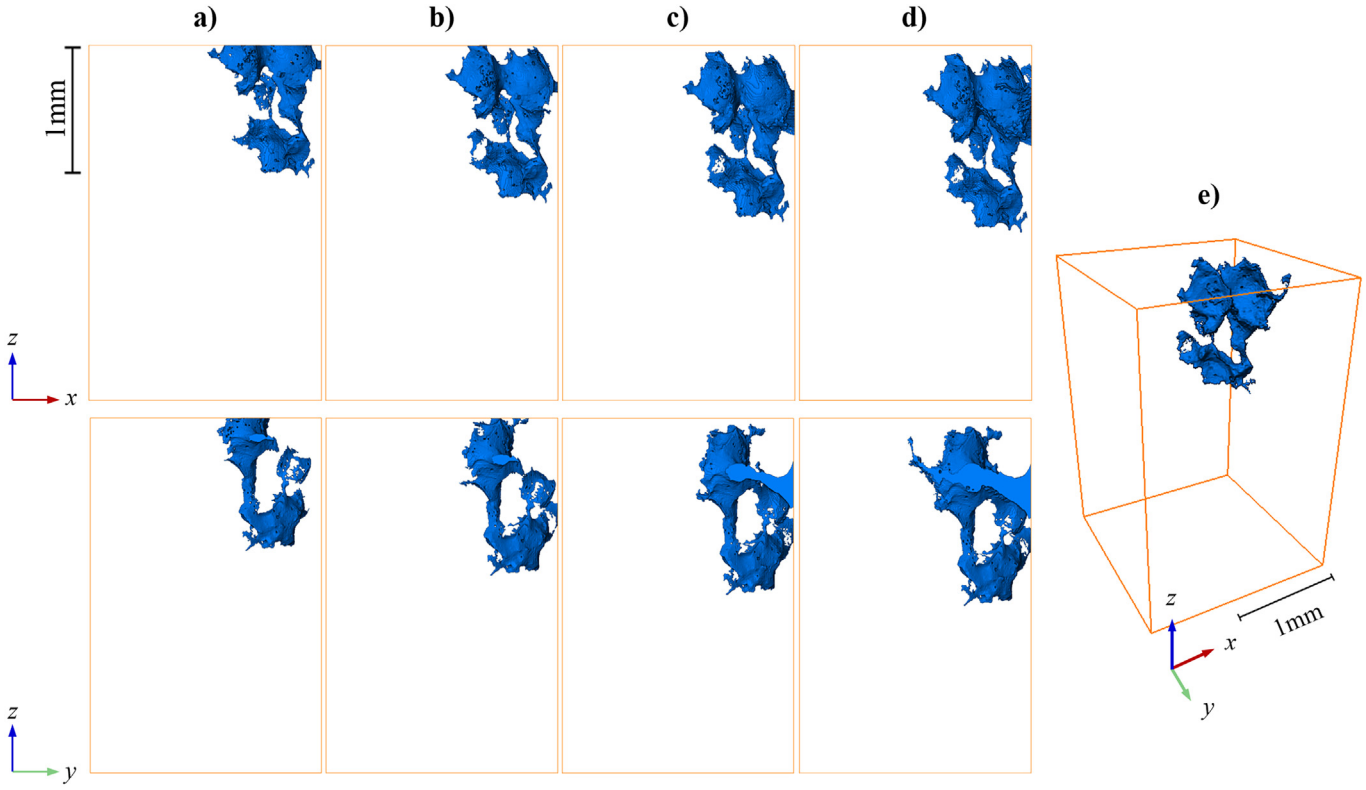

Fig. 16. Largest pore in HT6 middle section at increasing extension (*xz* and *yz* views): 0 (a), 0.43 (b), 0.7 (c) and 0.8 mm (d); perspective view at 0.8 mm (e).

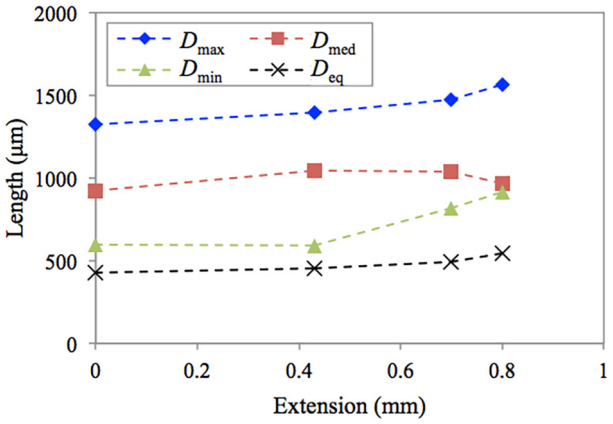

Fig. 17. Feret caliper dimensions of largest pore in HT6 middle section at increasing extension (figure available in colour online).

samples occurs by necking down of the material between adjacent voids and by localised shearing deformation bands between separated voids.

Feret caliper dimensions for the largest volume pore in H-1 at increasing extension are shown in Fig. 15a. Between 0 and 1.65 mm the longest dimension, orientated towards the loading direction, is elongated by 28.1% and the breadth is reduced by 22.4%. The third dimension remains fairly constant during this period (+2.1%), *i.e.* the pore becomes longer and flatter. The equivalent diameter increases by 19.6% from 0 to 1.65 mm, although the initial increase to 1 mm is only 4.0%, indicating pore shape modification occurs largely without volume change at small extension. The diameter then increases as damage propagates between 1.65 and 1.85 mm and all pore dimensions rise dramatically due to void growth and coalescence. Feret dimensions for the largest pore in the H-2 middle section are shown in Fig. 15b. The pore is elongated by 51.7% in the *z* direction at 1.65 mm before the significant void growth occurring between 1.65 and 1.75 mm. The lengths of D_{med} and D_{min} also appear to increase prior to the onset of damage, however there is uncertainty with transverse measurements owing to the pore's location at the edge of the sub-volume (top right of *xz* and *yz* views in Fig. 13). Like before, the equivalent diameter increases by 30.9% from 0 to 1.65 mm but increases by only 9.5% in the first 1.05 mm. We again note uncertainty due to potential shifting in/out of view.

Images and Feret dimensions of the largest pore located in the middle section of HT6 at increasing extension are shown in Figs. 16 and 17 respectively (the pore lies partially in the top sub-volume at 0 mm but the full pore is measured). From 0 to 0.43 mm the pore is elongated in the *z* direction and widened as damage visibly starts to develop from the edge of the sub-volume. There is an increase in D_{min} as the void grows from 0.43 mm to the final scanning extension. A reduction in D_{med} is attributed to the location of the pore at the edge of the sub-volume and lateral shifting of the pore partly out of view. Compared to the HIPped specimens, damage begins to visibly propagate earlier but extensive void growth and coalescence is not observed at the final scanning increment (94.2% of fracture extension) due to less ductile failure.

4. Conclusions

In this paper, sub-optimal AlSi10Mg specimens were fabricated by LPBF using recycled powder in order to study pores of significant size. The evolution of internal porosity was analysed by *in-situ* tensile testing with incremental XμCT scanning at increasing extension. Specimens were tested in as-built, HIPped and HIPped + T6'd conditions.

The total volume, quantity and shape of pores within brittle-like as-built specimens exhibiting small failure elongation were unchanged at the final *in-situ* scanning increments (over 90% of fracture extension). Porosity volume within ductile HIPped specimens increased uniformly under tension up to the onset of substantial void growth and

accumulation, at which point porosity drastically increased primarily in the region where the specimens split. An increase in pore frequency is likely the result of reopening of small pores initially collapsed by HIPping. Large pores that remained open were elongated in the loading direction and transversely flattened before void growth development, with shape change occurring largely without volume variation at small extension. Prominent pores in the vicinity of initial damage appeared to dictate the path of void growth. The tensile response and pore evolution for HIPped specimens with markedly different porosity (1.10% and 0.28%) was not appreciably different. Damage propagation began visibly earlier within the HIPped + T6'd specimen, however substantial void growth and coalescence was not observed in the build up to less ductile failure.

The approach outlined here can be used to investigate the evolution of pores of different size, shape and orientation within AlSi10Mg and other alloys processed using varying LPBF parameters and build conditions.

Declaration of Competing Interest

The authors declare that they have no known competing financial interests or personal relationships that could have appeared to influence the work reported in this paper.

Acknowledgements

The authors gratefully acknowledge the financial support of the Engineering and Physical Sciences Research Council (EPSRC) under grant reference EP/R021694/1, "3D in-situ based methodology for optimizing the mechanical performance of selective laser melted aluminium alloys".

CRediT author statement

James Hastie: Heat treatment, image post-processing, data analysis and drafting the manuscript.

Joachim Koelblin: Image post-processing, visualization, reviewing and editing the manuscript.

Mehmet Kartal: Conceptualization, funding acquisition, performing X-ray experiments, supervision, reviewing and editing the manuscript.

Moataz Attallah: Providing the lab facilities and materials, consulting, reviewing and editing the manuscript.

Rafael Martinez: Manufacturing the samples and heat treatment.

References

[1] I. Gibson, D. Rosen, B. Stucker, Additive Manufacturing Technologies: 3D Printing, Springer, Rapid Prototyping, New York Heidelberg Dordrecht London, 2014.
[2] T. DebRoy, H.L. Wei, J.S. Zuback, T. Mukherjee, J.W. Elmer, J.O. Milewski, A.M. Beese, A. Wilson-Heid, A. De, W. Zhang, Additive manufacturing of metallic components – process, structure and properties, Prog. Mater. Sci. 92 (2018) 112–224.
[3] E.O. Olakanmi, R.F. Cochrane, K.W. Dalgarno, A review on selective laser sintering/melting (SLS/SLM) of aluminium alloy powders: processing, microstructure, and properties, Prog. Mater. Sci. 74 (2015) 401–477.
[4] S.L. Sing, W.Y. Yeong, Laser powder bed fusion for metal additive manufacturing: perspectives on recent developments, Virtual and Physical Prototyping 15 (3) (2020) 359–370.
[5] J. L. Leirmo and I. Baturynska, "Challenges and proposed solutions for aluminium in laser powder bed fusion," in *53rd CIRP Conference on Manufacturing Systems*, Chicago, USA, 2020.
[6] M. Zavala-Arredondo, T. London, M. Allen, T. Maccio, S. Ward, D. Griffiths, A. Allison, P. Goodwin, C. Hauser, Use of power factor and specific point energy as design parameters in laser powder-bed-fusion (L-PBF) of AlSi10Mg alloy, Mater. Des. 182 (2019) 108018.
[7] N. Read, W. Wang, K. Essa, M.M. Attallah, Selective laser melting of AlSi10Mg alloy: process optimisation and mechanical properties development, Mater. Des. 65 (2015) 417–424.
[8] E. Louvis, P. Fox, C.J. Sutcliffe, Selective laser melting of aluminium components, J. Mater. Process. Technol. 211 (2) (2011) 275–284.
[9] N.T. Aboulkhair, N.M. Everitt, I. Ashcroft, C. Tuck, Reducing porosity in AlSi10Mg parts processed by selective laser melting, Additive Manufacturing 1-4 (2014) 77–86.
[10] K. Kempen, L. Thijs, J. Van Humbeeck, J.-P. Kruth, Processing AlSi10Mg by selective laser melting: parameter optimisation and material characterisation, Mater. Sci. Technol. 31 (8) (2015) 917–923.
[11] J.C. Hastie, M.E. Kartal, L.N. Carter, M.M. Attallah, D.M. Mulvihill, Classifying shape of internal pores within AlSi10Mg alloy manufactured by laser powder bed fusion using 3D X-ray micro computed tomography: influence of processing parameters and heat treatment, Mater. Charact. 163 (2020) 110225.
[12] N.O. Larrosa, W. Wang, N. Read, M.H. Loretto, C. Evans, J. Carr, U. Tradowsky, M.M. Attallah, P.J. Withers, Linking microstructure and processing defects to mechanical properties of selectively laser melted AlSi10Mg alloy, Theor. Appl. Fract. Mech. 98 (2018) 123–133.
[13] E.O. Olakanmi, Selective laser sintering/melting (SLS/SLM) of pure Al, Al-mg, and Al-Si powders: effect of processing conditions and powder properties, J. Mater. Process. Technol. 213 (8) (2013) 1387–1405.
[14] L.F. Wang, J. Sun, X.L. Yu, Y. Shi, X.G. Zhu, L.Y. Cheng, H.H. Liang, B. Yan, L.J. Guo, Enhancement in mechanical properties of selectively laser-melted AlSi10Mg aluminum alloys by T6-like heat treatment, Materials Science & Engineering A 734 (2018) 299–310.
[15] W.H. Kan, Y. Nadot, M. Foley, L. Ridosz, G. Proust, J.M. Cairney, Factors that affect the properties of additively-manufactured AlSi10Mg: porosity versus microstructure, Additive Manufacturing 29 (2019) 100805.
[16] L. Zhao, J.G. Santos Macías, L. Ding, H. Idrissi, A. Simar, Damage mechanisms in selective laser melted AlSi10Mg under as built and different post-treatment conditions, Materials Science & Engineering A 764 (2019) 138210.
[17] L. Thijs, K. Kempen, J.-P. Kruth, P. Van Humbeeck, Fine-structured aluminium products with controllable texture by selective laser melting of pre-alloyed AlSi10Mg powder, Acta Mater. 61 (5) (2013) 1809–1819.
[18] N.T. Aboulkhair, I. Maskery, C. Tuck, I. Ashcroft, N.M. Everitt, The microstructure and mechanical properties of selectively laser melted AlSi10Mg: the effect of a conventional T6-like heat treatment, Mater. Sci. Eng. A 667 (2016) 139–146.
[19] M. Giovagnoli, M. Tocci, A. Fortini, M. Merlin, M. Ferroni, A. Migliori, A. Pola, Effect of different heat-treatment routes on the impact properties of an additively manufactured AlSi10Mg alloy, Mater. Sci. Eng. A 802 (2021) 140671.
[20] T. Hirata, T. Kimura, T. Nakamoto, Effects of hot isostatic pressing and internal porosity on the performance of selective laser melted AlSi10Mg alloys, Mater. Sci. Eng. A 772 (2020) 138713.
[21] W. Li, S. Li, J. Liu, A. Zhang, Y. Zhou, Q. Wei, C. Yan, Y. Shi, Effect of heat treatment on AlSi10Mg alloy fabricated by selectivelaser melting: microstructure evolution, mechanical properties and fracture mechanism, Materials Science & Engineering A 663 (2016) 116–125.
[22] N. Takata, H. Kodaira, K. Sekizawa, A. Suzuki, M. Kobashi, Change in microstructure of selectively laser melted AlSi10Mg alloy with heat treatments, Mater. Sci. Eng. A 704 (2017) 218–228.
[23] I. Rosenthal, R. Shneck, A. Stern, Heat treatment effect on the mechanical properties and fracture mechanism in AlSi10Mg fabricated by additive manufacturing selective laser melting process, Mater. Sci. Eng. A 729 (2018) 310–322.
[24] L.-Z. Wang, S. Wang, J.-J. Wu, Experimental investigation on densification behavior and surface roughness of AlSi10Mg powders produced by selective laser melting, Opt. Laser Technol. 96 (1) (2017) 88–96.
[25] W. Pei, W. Zhengying, C. Zhen, D. Jun, H. Yuyang, L. Junfeng, Z. Yatong, The AlSi10Mg samples produced by selective laser melting: singletrack, densification, microstructure and mechanical behavior, Appl. Surf. Sci. 408 (2017) 38–50.
[26] A. du Plessis, I. Yadroitsev, I. Yadroitsava, S.G. Le Roux, X-ray microcomputed tomography in additive manufacturing: a review of the current technology and applications, 3D Printing and Additive Manufacturing 5 (3) (2018) 227–247.
[27] A. du Plessis, I. Yadroitsava, I. Yadroitsev, Effects of defects on mechanical properties in metal additive manufacturing: a review focusing on X-ray tomography insights, Mater. Des. 187 (2020) 108385.
[28] A. du Plessis, Effects of process parameters on porosity in laser powder bed fusion revealed by X-ray tomography, Additive Manufacturing 30 (2019) 100871.
[29] Z. Dong, X. Zhang, W. Shi, H. Zhou, H. Lei and J. Liang, "Study of size effect on microstructure and mechanical properties of AlSi10Mg samples made by selective laser melting," *Materials*, vol. 11, no. 12, p. 2463, 2018.
[30] S. Romano, A. Abel, J. Gumpinger, A.D. Brandão, S. Beretta, Quality control of AlSi10Mg produced by SLM: metallography versus CT scans for critical defect size assessment, Additive Manufacturing 28 (2019) 394–405.
[31] H. Lei, C. Li, J. Meng, H. Zhou, Y. Liu, X. Zhang, P. Wang, D. Fang, Evaluation of compressive properties of SLM-fabricated multi-layer lattice structures by experimental test and μ-CT-based finite element analysis, Mater. Des. 169 (2019) 107685.
[32] U. Tradowsky, J. White, R.M. Ward, N. Read, W. Reimers, M.M. Attallah, Selective laser melting of AlSi10Mg: influence of post-processing on the microstructural and tensile properties development, Mater. Des. 105 (2016) 212–222.
[33] A.L. Gurson, Continuum theory of ductile rupture by void nucleation and growth: part I—yield criteria and flow rules for porous ductile media, J. Eng. Mater. Technol. 99 (1) (1977) 2–15.
[34] V. Tvergaard, A. Needleman, Analysis of the cup-cone fracture in a round tensile bar, Acta Metall. 32 (1) (1984) 157–169.
[35] U.B. Asim, M.A. Siddiq, M.E. Kartal, A CPFEM based study to understand the void growth in high strength dual-phase titanium alloy (Ti-10V-2Fe-3Al), Int. J. Plast. 122 (2019) 188–211.
[36] U. B. Asim, M. A. Siddiq and M. Demiral, "Void growth in high strength aluminium alloy single crystals: a CPFEM based study," *Modelling and Simulation in Materials Science and Engineering*, vol. 25, no. 3, p. 035010, 2017.

[37] H.D. Carlton, A. Haboub, G.F. Gallegos, D.Y. Parkinson, A.A. MacDowell, Damage evolution and failure mechanisms in additively manufactured stainless steel, Mater. Sci. Eng. A 651 (2016) 406–414.
[38] F.H. Kim, S.P. Moylan, T.Q. Phan, E.J. Garboczi, Investigation of the effect of artificial internal defects on the tensile behavior of laser powder bed fusion 17–4 stainless steel samples: simultaneous tensile testing and X-ray computed tomography, Exp. Mech. 60 (2020) 987–1004.
[39] J. Samei, M. Amirmaleki, A.P. Ventura, G.T. Pawlikowski, M. Bayes, W.Z. Misiolek, D.S. Wilkinson, In-situ X-ray tomography analysis of the evolution of pores during deformation of a cu-Sn alloy fabricated by selective laser melting, Additive Manufacturing 34 (2020) 101196.
[40] J. Samei, M. Amirmaleki, M.S. Dastgiri, C. Marinelli, In-situ X-ray tomography analysis of the evolution of pores during deformation of AlSi10Mg fabricated by selective laser melting, Mater. Lett. 255 (2019) 126512.
[41] Y. Nadot, C. Nadot-Martin, W.H. Kan, S. Boufadene, M. Foley, J. Cairney, G. Proust, L. Ridosz, Predicting the fatigue life of an AlSi10Mg alloy manufactured via laser powder bed fusion by using data from computed tomography, Additive Manufacturing 32 (2020) 100899.
[42] R.M. Molak, M.E. Kartal, Z. Pakiela, K.J. Kurzydlowski, The effect of specimen size and surface conditions on the local mechanical properties of 14MoV6 ferritic–pearlitic steel, Mater. Sci. Eng. A 651 (2016) 810–821.
[43] R.M. Molak, M.E. Kartal, Z. Pakiela, W. Manaj, M. Turski, S. Hiller, S. Gungor, L. Edwards, K.J. Kurzydlowski, Use of micro tensile test samples in determining the remnant life of pressure vessel steels, Appl. Mech. Mater. 7-8 (2007) 187–194.
[44] M.B. Prime, Cross-sectional mapping of residual stresses by measuring the surface contour after a cut, J. Eng. Mater. Technol. 123 (2) (2001) 162–168.
[45] M.J. Madou, Fundamentals of Microfabrication: The Science of Miniaturization, CRC Press, Boca Raton, 2002.
[46] "VersaXRM-410," Xradia, Inc, [Online]. Available: https://www.zeiss.com/microscopy. [Accessed 19 08 2020].
[47] "In-Situ tensile/compression testing stages for micro x-ray computed tomography," Deben, UK, [Online]. Available: https://deben.co.uk/. [Accessed 19 08 2020].
[48] M.E. Kartal, L.H. Dugdale, J.J. Harrigan, M.A. Siddiq, D. Pokrajac, D.M. Mulvihill, Three-dimensional in situ observations of compressive damage mechanisms in syntactic foam using X-ray microcomputed tomography, J. Mater. Sci. 52 (2017) 10186–10197.